Biaxial disclinated states in nematic elastomers

Eliot Fried, Vladimir Korchagin & Russell E. Todres
Department of Theoretical and Applied Mechanics
University of Illinois at Urbana-Champaign
Urbana, IL 61801-2935, USA

Abstract

We use a continuum model to investigate the isochoric axial contraction and expansion of a right circular cylindrical specimen composed of a nematic elastomer that is cross-linked in a uniaxial state and then annealed. We build on previous work by relaxing the constraint that the molecular conformation be spherical or uniaxial, allowing instead for biaxiality. The material exhibits an energetic preference for states involving a disclination of strength +1 along the cylinder axis surrounded by a region in which the conformation of the polymer chains is indeed biaxial. We show that such states represent minimizers of the total free-energy. Also, the reactive pressure necessary to enforce the constraint of material incompressibility within the disclination core is found to be reduced by an order of magnitude when the conformation is biaxial rather than uniaxial. A bifurcation analysis is used to analytically determine the thresholds of axial expansion and contraction at which the material prefers a disclinated state. These thresholds are found to be consistent with numerical predictions. Finally, the stability of the solutions for the studied parameters is also investigated.

Keywords: disclinations; elastomers; liquid-crystalline polymers (LCP); nematic; microstructure

1 Introduction

Disclinations and defects play an important role in traditional nematic liquid crystals and are expected to be equally influential in nematic elastomers. Previously,[1–3] we used a continuum model to investigate both the existence and detection of disclinations of strength +1 induced by the isochoric distortion of a right circular cylindrical specimen composed of a nematic elastomer that is cross-linked in a uniaxial state and then annealed. Under deformation, rather than remaining in its annealed, isotropic, reference state, we found that there is an energetic preference for the material to achieve a disclinated state consisting of an isotropic core surrounded by an anisotropic region in which the conformation of polymer chains was uniaxial. Furthermore, by investigating the first normal-stress difference, we proposed a practical method for detecting the onset of a disclinated state.

Our previous work only allowed for a uniaxial molecular conformation. Here, although prepared with a uniaxial conformation as before, the polymer chains are permitted to take on biaxial conformations. From our earlier investigations, we know that, when sufficiently deformed, a nematic-elastomeric cylinder will exhibit a disclination. This work is motivated by the question as to whether the conformation of polymer chains in the region surrounding the core of such a disclination is uniaxial or become biaxial. If this extra-core region is uniaxial, there is then no need to allow for biaxiality. However, if

this extra-core region is biaxial, we can conclude that a model in which the conformation is constrained to be either sperhical or uniaxial overly restrictive and that allowing for biaxiality is a necessary refinement.

To describe biaxiality, we introduce scalar asphericities $q_1 > -1$ and $q_2 > -1$ and associated unit orientations $\boldsymbol{n}_1$ and $\boldsymbol{n}_2$. The chains are: oblate about $\boldsymbol{n}_1$ for $-1 < q_1 < 0$; spherical for $q_1 = 0$; and prolate about $\boldsymbol{n}_1$ for $q > 0$. Analogous interpretations hold for q_2 and $\boldsymbol{n}_2$. In our theory, the asphericities and orientations have the status of additional kinematical degrees of freedom. These lead to balances for aspherical and orientational forces that are enforced in addition to the standard balance associated with the deformational balance. The first asphericity q_1 and orientation $\boldsymbol{n}_1$ correspond to q and $\boldsymbol{n}$ in our previous work.[1–3] Thus, if in deforming a nematic elastomeric cylinder, we find that $q_1 \neq 0$ and $q_2 = 0$ in the extra-core region, we can infer that the disclination is uniaxial. However, if both $q_1 \neq 0$ and $q_2 \neq 0$ in the extra-core region, the disclination is biaxial.

In fact, for both radial expansion and contraction of such a cylinder, we do indeed discover disclinated states in which the conformation of the region surrounding the core is biaxial. Such states possess lower total free-energy than those in which the conformation is uniaxial or isotropic. Thus, we find that there is an energetic incentive for disclinated states involving an extra-core region that is biaxially rather than uniaxially anisotropic. Furthermore, we find that in a biaxially disclinated state the pressure necessary to maintain the constraint of material incompressibility within the disclination core is generally an order of magnitude less than that necessary in a uniaxially disclinated state.

These results are obtained via numerical studies of the governing boundary-value problem. To explore their basis, we perform bifurcation and stability analyses of the underlying differential equations. These analyses yield expressions for the threshold values of axial contraction and expansion for which biaxial states are preferred and these expressions confirm our numerical results.

2 Theory

The kinematical description of a nematic elastomer involves two fields: the vector-valued deformation $\boldsymbol{y}$ and the positive-definite and symmetric molecular conformation $\boldsymbol{A}$, a macroscopic measure of the nematically-induced distortion of the polymer chains comprising the network. Associated with $\boldsymbol{y}$ is the deformation-gradient $\boldsymbol{F} = \operatorname{Grad} \boldsymbol{y}$, which serves as a macroscopic measure of the distortion of the network. Assuming that the medium is incompressible, we must have $\det \boldsymbol{F} = 1$. Being positive-definite and symmetric, $\boldsymbol{A}$ in general possesses three distinct eigenvalues and eigenvectors and, thus, may be spherical, uniaxial, or biaxial. When $\boldsymbol{A}$ is spherical, the medium behaves as conventional isotropic rubber. Otherwise, the optical-mechanical response of the material is anisotropic. In general, we may represent $\boldsymbol{A}$ in the form

$$\boldsymbol{A} = a(1+q_1)^{-\frac{1}{3}}(1+q_2)^{-\frac{1}{3}}(\boldsymbol{1} + q_1 \boldsymbol{n}_1 \otimes \boldsymbol{n}_1 + q_2 \boldsymbol{n}_2 \otimes \boldsymbol{n}_2), \tag{1}$$

with $\det \boldsymbol{A} = a > 0$, scalar asphericities $q_\beta > -1$, $\beta = 1, 2$, and orientations $\boldsymbol{n}_\beta$ which are orthogonal ($\boldsymbol{n}_1 \cdot \boldsymbol{n}_2 = 0$) and of unit length ($|\boldsymbol{n}_\beta| = 1$). The polymer chains are prolate, spherical, or oblate about $\boldsymbol{n}_\beta$ as $-1 < q_\beta < 0$, $q_\beta = 0$, or $q_\beta > 0$, respectively.

Within the molecular-statistical framework of Warner et al.,[21] the coupling between the kinematical degrees of freedom is embodied by a free-energy density of the form

$$\tfrac{1}{2}\mu(|\boldsymbol{A}^{-\frac{1}{2}}\boldsymbol{F}\boldsymbol{\Lambda}^{\frac{1}{2}}|^2 - \ln\det(\boldsymbol{A}^{-1}\boldsymbol{\Lambda}) - 3). \tag{2}$$

Here, $\mu > 0$ is the shear modulus and $\boldsymbol{\Lambda}$ is the positive-definite and symmetric molecular conformation at the time of cross-linking. While μ would be determined by conventional

mechanical tests, $\boldsymbol{\Lambda}$ would be determined using scattering methods. When $\boldsymbol{A} = \boldsymbol{\Lambda} = \alpha \boldsymbol{1}$, (2) reduces to the classical expression $\frac{1}{2}\mu(|\boldsymbol{F}|^2 - 3)$ of neo-Hookean rubber elasticity.

We consider a nematic elastomer formed by a two-step process as follows: first, the melt is cross-linked in a uniaxial state with asphericity $q_* \neq 0$ and unit orientation $\boldsymbol{n}_*$; next, the resulting network is annealed, giving rise to an isotropic reference state in which the conformation at each material point is of the spherical form $\boldsymbol{\Lambda} = \alpha \boldsymbol{1}$. In addition to possessing an energetic preference for the isotropic reference state, we assume that the material possesses an energetic preference for states in which either or both of the asphericities adopt the value q_* present at the time of cross-linking. However, we assume that the annealing process renders negligible any energetic preference for the orientation axis $\boldsymbol{n}_*$ of the molecular conformation at the time of cross-linking. To describe such a material, we incorporate (2) and consider a free-energy density of the form

$$\psi = \frac{\mu}{2}\Big((1+q_1)^{\frac{1}{3}}(1+q_2)^{\frac{1}{3}}\Big(|\boldsymbol{F}|^2 - \frac{q_1}{1+q_1}|\boldsymbol{F}^\top \boldsymbol{n}_1|^2 - \frac{q_2}{1+q_2}|\boldsymbol{F}^\top \boldsymbol{n}_2|^2\Big) - 3\Big) + \Phi(q_1, q_2)$$
$$+2\delta q_1(q_1 - q_*)q_2(q_2 - q_*) + \frac{\alpha}{2}(|\boldsymbol{h}_1|^2 + |\boldsymbol{h}_2|^2) + \Gamma(q_1)K(\boldsymbol{F}, \boldsymbol{n}_1, \boldsymbol{G}_1) + \Gamma(q_2)K(\boldsymbol{F}, \boldsymbol{n}_2, \boldsymbol{G}_2). \tag{3}$$

Here, $\boldsymbol{G}_\beta = \operatorname{Grad} \boldsymbol{n}_\beta$ is the gradient of the orientation $\boldsymbol{n}_\beta$; Φ is a quadruple-well potential, with minima at $(q_1, q_2) = (0, 0)$, $(q_1, q_2) = (0, q_*)$, $(q_1, q_2) = (q_*, 0)$, and $(q_1, q_2) = (q_*, q_*)$, consistent with

$$\Phi(q_1, q_2) \to +\infty \quad \text{as } q_1 \to -1, +\infty \quad \text{or} \quad q_2 \to -1, +\infty; \tag{4}$$

$\delta \geq 0$ is a mixing coefficient; $\boldsymbol{h}_\beta = \operatorname{Grad} q_\beta$ is the gradient of the asphericity q_β; $\alpha > 0$ is a *regularizing modulus*; Γ is a mollifying factor, dimensionless and consistent with

$$\left.\begin{aligned} \Gamma(q) = O(q^2) \quad &\text{as } q \to 0, \\ \Gamma(q) > 0 \quad &\text{for } q \neq 0, \\ \Gamma(q) \to +\infty \quad &\text{as } q \to -1, +\infty; \end{aligned}\right\} \tag{5}$$

and K, involving *orientational-elasticity moduli* $\kappa_1 > 0$, $\kappa_2 > 0$, $\kappa_3 > 0$, $\kappa_4 > 0$, and $\kappa_5 > 0$, is a generalization of the energy density of the Oseen–Zöcher–Frank (OZF) theory to account for deformation.

The first term of the right side of (3) arises from (2) on taking $\boldsymbol{A}$ as given in (1) and $\boldsymbol{\Lambda} = \alpha \boldsymbol{1}$. The factor K appearing in the remaining terms on the right side of (3) is of the form

$$K(\boldsymbol{F}, \boldsymbol{n}, \boldsymbol{G}) = \frac{\kappa_1}{2}(\boldsymbol{F} \cdot \boldsymbol{G})^2 + \frac{\kappa_2}{2}|\boldsymbol{F}^\top \boldsymbol{G}|^2 + \frac{\kappa_3(|\boldsymbol{F}^\top \boldsymbol{G}\boldsymbol{F}^\top \boldsymbol{n}|^2 + |\boldsymbol{G}^\top \boldsymbol{F}\boldsymbol{F}^\top \boldsymbol{n}|^2)}{2|\boldsymbol{F}^\top \boldsymbol{n}|^2}$$
$$+ \frac{\kappa_4}{2}(\boldsymbol{F}^\top \boldsymbol{G}) \cdot (\boldsymbol{G}^\top \boldsymbol{F}) + \frac{\kappa_5(\boldsymbol{F}^\top \boldsymbol{G}\boldsymbol{F}^\top \boldsymbol{n}) \cdot (\boldsymbol{G}^\top \boldsymbol{F}\boldsymbol{F}^\top \boldsymbol{n})}{2|\boldsymbol{F}^\top \boldsymbol{n}|^2}. \tag{6}$$

On setting $\boldsymbol{F} = \boldsymbol{1}$ in (6), we may identify $\kappa_1 + \kappa_2 + \kappa_4$, κ_2, $\kappa_2 + \kappa_3$, and $\kappa_2 + \kappa_4$ with the classical splay, twist, bend, and saddle-splay moduli of the OZF theory; $\kappa_3 + \kappa_5$ is an additional modulus that accounts for interactions between the distortion of the network and the orientation of the molecular conformation. By (4) and (5), both Φ and Γ penalize states in which the conformation becomes overly oblate or prolate about any axis.

Within our framework, a disclination in a nematic elastomer is a tubular neighborhood within which the asphericity vanishes and the orientation is undefined. The orientation gradient and, hence, K are therefore singular within such a neighborhood. The mollifying

factor Γ appearing in the final two terms on the right side of (3) is introduced to render integrable any such singularities.[17]

If we restrict attention to states in which the asphericity is uniaxial, so that, without loss of generality, $q_1 \equiv q \neq 0$, $q_2 \equiv 0$, $\boldsymbol{n}_1 \equiv \boldsymbol{n}$, and $\boldsymbol{n}_2$ is undefined, then the free-energy density (3) reduces to the expression considered earlier.[1–3]

Granted (3) and that external body forces are absent, the variationally-based equilibrium equations of the theory are:

$$\left.\begin{aligned} \mathrm{Div}\Big(\frac{\partial \psi}{\partial \boldsymbol{F}}\Big) &= \boldsymbol{F}^{-\top}\mathrm{Grad}\, p, \\ \mathrm{Div}\Big(\frac{\partial \psi}{\partial \boldsymbol{h}_1}\Big) &= \frac{\partial \psi}{\partial q_1}, \\ \mathrm{Div}\Big(\frac{\partial \psi}{\partial \boldsymbol{h}_2}\Big) &= \frac{\partial \psi}{\partial q_2}, \\ \mathrm{Div}\Big(\frac{\partial \psi}{\partial \boldsymbol{G}_1}\Big) + \Big(\frac{\partial \psi}{\partial \boldsymbol{G}_1}\cdot \boldsymbol{G}_1\Big)\boldsymbol{n}_1 &= \frac{\partial \psi}{\partial \boldsymbol{n}_1}, \\ \mathrm{Div}\Big(\frac{\partial \psi}{\partial \boldsymbol{G}_2}\Big) + \Big(\frac{\partial \psi}{\partial \boldsymbol{G}_2}\cdot \boldsymbol{G}_2\Big)\boldsymbol{n}_2 &= \frac{\partial \psi}{\partial \boldsymbol{n}_2}, \end{aligned}\right\} \tag{7}$$

where all differentiation of ψ is performed on the manifold associated with the constraints $\det \boldsymbol{F} = 1$ and $|\boldsymbol{n}_\beta| = 1$, $\beta = 1, 2$, and where p denotes the pressure required to maintain the constraint $\det \boldsymbol{F} = 1$. While $(7)_1$ expresses conventional balance of force associated with $\boldsymbol{y}$, $(7)_2$, $(7)_3$, $(7)_4$, and $(7)_5$ express generalized force balances associated, respectively, with the additional kinematical degrees of freedom q_1, q_2, $\boldsymbol{n}_1$, and $\boldsymbol{n}_2$.

Following the approach taken in previous work,[1–3] we use the theory to investigate the presence of disclinations of strength $+1$ in a nematic-elastomeric specimen that, in the reference state, occupies the right circular cylinder

$$\mathcal{R} = \{\boldsymbol{x} = r\boldsymbol{e}_r + z\boldsymbol{e}_z : 0 \leq r < R, |z| < \infty\}, \tag{8}$$

with cylindrical coordinates (r, θ, z) and $\{\boldsymbol{e}_r, \boldsymbol{e}_\theta, \boldsymbol{e}_z\}$ the associated physical basis. In so doing, we assume that the lateral surface $\partial\mathcal{R} = \{\boldsymbol{x} : |\boldsymbol{x}| = R\}$ of the specimen is free of all tractions, viz.,

$$\left.\begin{aligned} \Big(\frac{\partial \psi}{\partial \boldsymbol{F}} - p\boldsymbol{F}^{-\top}\Big)\Big|_{\partial\mathcal{R}}\boldsymbol{e}_r &= \boldsymbol{0}, \\ \frac{\partial \psi}{\partial \boldsymbol{h}_\beta}\Big|_{\partial\mathcal{R}}\cdot \boldsymbol{e}_r = 0, \qquad \frac{\partial \psi}{\partial \boldsymbol{G}_\beta}\Big|_{\partial\mathcal{R}}\boldsymbol{e}_r &= \boldsymbol{0},\ \beta = 1{,}2. \end{aligned}\right\} \tag{9}$$

Consistent with the requirement that the deformation be isochoric, we stipulate that

$$\boldsymbol{y}(r, \theta, z) = \lambda r\boldsymbol{e}_r + \frac{z}{\lambda^2}\boldsymbol{e}_z, \quad \text{with} \quad \lambda > 0. \tag{10}$$

The case of $0 < \lambda < 1$ corresponds to radial contraction coupled with axial extension of the cylinder, while that of $\lambda > 1$ is compatible with the cylinder expanding radially while contracting along its axis. From (10),

$$\boldsymbol{F}(r, \theta, z) = \lambda(\boldsymbol{1} - \boldsymbol{e}_z\otimes\boldsymbol{e}_z) + \frac{1}{\lambda^2}\boldsymbol{e}_z\otimes\boldsymbol{e}_z, \tag{11}$$

and a direct calculation shows that, for all $\lambda > 0$, the constraint $\det \boldsymbol{F} = 1$ holds throughout $\mathcal{R}$.

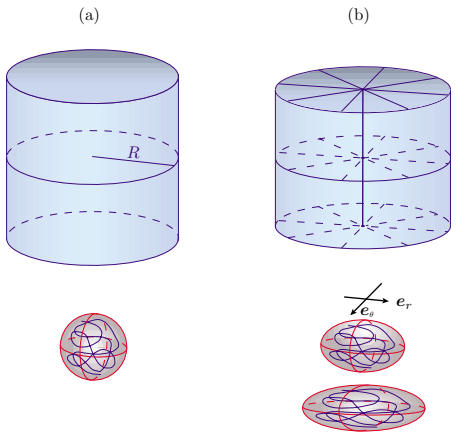

Figure 1: Cylinder and molecular conformation in undistorted (a) and distorted (b) states.

When $q_\beta = 0$, the orientation $\boldsymbol{n}_\beta$ is undefined. When $q_1 \neq 0$, we assume that $\boldsymbol{n}_1$ is radial, so that

$$\boldsymbol{n}_1 = \boldsymbol{e}_r. \tag{12}$$

Further, when $q_2 \neq 0$, we suppose that $\boldsymbol{n}_2$ is azimuthal, so that

$$\boldsymbol{n}_2 = \boldsymbol{e}_\theta. \tag{13}$$

As a consequence of these choices, the constraint $|\boldsymbol{n}_\beta| = 1$ is satisfied whenever $\boldsymbol{n}_\beta$ is defined. A direct calculation shows that, when $\boldsymbol{n}_1$ and $\boldsymbol{n}_2$ are defined,

$$\left.\begin{aligned} \boldsymbol{G}_1(r,\theta,z) &= \frac{1}{r}\boldsymbol{e}_\theta \otimes \boldsymbol{e}_\theta, \\ \boldsymbol{G}_2(r,\theta,z) &= -\frac{1}{r}\boldsymbol{e}_r \otimes \boldsymbol{e}_\theta. \end{aligned}\right\} \tag{14}$$

Further, we suppose that the asphericities q_1 and q_2 depend at most on the radial coordinate r.

Using (6) and (11)–(14) gives

$$\left.\begin{aligned} K(\boldsymbol{F},\boldsymbol{n}_1,\boldsymbol{G}_1) &= \frac{\kappa_I \lambda^2}{2r^2}, \\ K(\boldsymbol{F},\boldsymbol{n}_2,\boldsymbol{G}_2) &= \frac{\kappa_{I\!I} \lambda^2}{2r^2}, \end{aligned}\right\} \tag{15}$$

with $\kappa_I = \kappa_1 + \kappa_2 + \kappa_4$ the *orientational splay modulus* and $\kappa_{I\!I} = \kappa_2 + \kappa_3$ the *orientational bend modulus*.

Since the deformation is prescribed via (10) and the orientations are either given as in (12) and (13) or undefined, the only unknowns are the pressure p and asphericities q_1 and q_2. From the radial component of $(7)_1$ and the assumption that q_1 and q_2 depend at most on r, it follows that p also may depend at most on r.

Letting ν be a parameter proportional to the height of the barrier separating the minima of the quadruple-well potential Φ and introducing $x = r/R$, $P(x) = p(Rx)/\nu$, and $Q_\beta(x) = q_\beta(Rx)$, $\beta = 1, 2$, we obtain the dimensionless groups

$$\mu^* = \frac{\mu}{\nu}, \quad \kappa_I^* = \frac{\kappa_I}{R^2\nu}, \quad \kappa_{I\!I}^* = \frac{\kappa_{I\!I}}{R^2\nu}, \quad \text{and} \quad \alpha^* = \frac{\alpha}{R^2\nu}. \tag{16}$$

Using the radial components of $(7)_1$ and $(9)_1$, we find that the dimensionless pressure P has the form

$$P = \lambda^2\Big(\mu^*\frac{(1+Q_2)^{\frac{1}{3}}}{(1+Q_1)^{\frac{2}{3}}} + \frac{\kappa_{I\!I}^*\Gamma(Q_2)}{x^2} + \mu^* I_1 + I_2\Big), \tag{17}$$

with

$$\left.\begin{aligned} I_1(x) &= \int_x^1 \frac{(Q_1(\xi)-Q_2(\xi))\,d\xi}{\xi(1+Q_1(\xi))^{\frac{2}{3}}(1+Q_2(\xi))^{\frac{2}{3}}},\\ I_2(x) &= \int_x^1 \frac{\big(\kappa_I^*\Gamma(Q_1(\xi)) - \kappa_{I\!I}^*\Gamma(Q_2(\xi))\big)\,d\xi}{\xi^3}. \end{aligned}\right\} \tag{18}$$

From $(7)_2$ and $(7)_3$, we obtain the differential equations

$$\left.\begin{aligned} \frac{\alpha^*}{x}\frac{d}{dx}\Big(x\frac{dQ_1}{dx}\Big) &= \frac{\mu^*\lambda^2(1+Q_2)^{\frac{1}{3}}}{6(1+Q_1)^{\frac{2}{3}}}\Big(\frac{1}{\lambda^6} - \frac{1-Q_1}{1+Q_1} - \frac{Q_2}{1+Q_2}\Big) + \frac{\kappa_I^*\lambda^2\Gamma'(Q_1)}{2x^2}\\ &\quad + \frac{1}{\nu}\frac{\partial\Phi(Q_1,Q_2)}{\partial Q_1} + \frac{2\delta}{\nu}(2Q_1-Q_*)Q_2(Q_2-Q_*),\\ \frac{\alpha^*}{x}\frac{d}{dx}\Big(x\frac{dQ_2}{dx}\Big) &= \frac{\mu^*\lambda^2(1+Q_1)^{\frac{1}{3}}}{6(1+Q_2)^{\frac{2}{3}}}\Big(\frac{1}{\lambda^6} - \frac{Q_1}{1+Q_1} - \frac{1-Q_2}{1+Q_2}\Big) + \frac{\kappa_{I\!I}^*\lambda^2\Gamma'(Q_2)}{2x^2}\\ &\quad + \frac{1}{\nu}\frac{\partial\Phi(Q_1,Q_2)}{\partial Q_2} + \frac{2\delta}{\nu}(2Q_2-Q_*)Q_1(Q_1-Q_*), \end{aligned}\right\} \tag{19}$$

which are augmented by the boundary conditions,

$$\frac{dQ_\beta}{dx}\Big|_{x=0} = 0 \quad \text{and} \quad \frac{dQ_\beta}{dx}\Big|_{x=1} = 0, \tag{20}$$

arising, respectively, from the assumed radial symmetry of the solution and $(9)_2$.

When $q_1 = 0$ and $\boldsymbol{n}_1$ is undefined, $(7)_4$ is vacuous. However, when $q_1 \neq 0$ and $\boldsymbol{n}_1$ is therefore defined, direct calculations show that $(7)_4$ is satisfied. Entirely analogous remarks hold concerning q_2, $\boldsymbol{n}_2$, and $(7)_5$.

3 Numerical results

The differential equation (19) involves functions Φ and Γ, which are restricted only by (4) and (5). Although many function choices would satisfy these restrictions, for consistency and ease of comparison with the uniaxial case, we took similar Φ and Γ for our numerical investigations as before,[1–3] viz.,

$$\Phi(q_1,q_2) = \frac{\nu q_1^2(q_1-q_*)^2}{2(1+q_1)^2} + \frac{\nu q_2^2(q_2-q_*)^2}{2(1+q_2)^2} \tag{21}$$

and

$$\Gamma(q) = \begin{cases} \dfrac{q^2}{(1+q)^2} & \text{if } -1 < q \le 0,\\[2ex] q^2 & \text{if } q \ge 0. \end{cases} \tag{22}$$

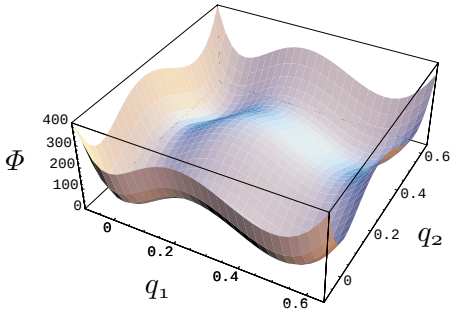

Figure 2: Plot of Φ, as defined in (21) for $\nu = 10^6$ J/m^3, $q_* = 0.5$, and $\delta = 0$.

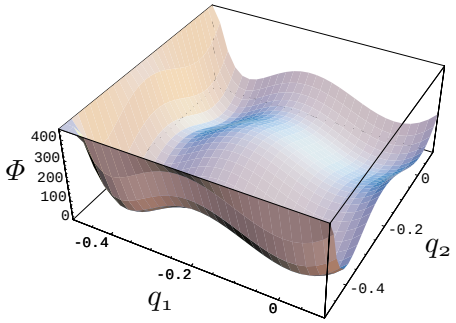

Figure 3: Plot of Φ, as defined in (21) for $\nu = 10^6$ J/m^3, $q_* = -0.4$, and $\delta = 0$.

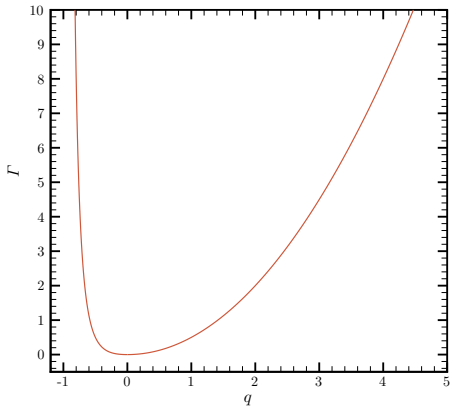

Figure 4: Plot of Γ, as defined in (22).

The mixing factor δ in (19) was taken to be 0 so that the wells of $\Phi(q_1, q_2)$ were of equal height.

To solve the boundary-value problem (19)–(20) numerically, we incorporated (21) and (22) and selected parameters as follows. As before,[1–3] we chose $\mu = 10^5$ J/m^3, $\nu = 10^6$ J/m^3, and $R = 1$ cm. Furthermore, for traditional nematics at temperatures in a wide range below the clearing temperature, the bend modulus $\kappa_{I\!I}$ is on the order of 10^{-12} J/m and is three-halves to twice the splay modulus κ_I.[22–25] The values of these moduli have not yet been determined for nematic elastomers, but because of the rubbery

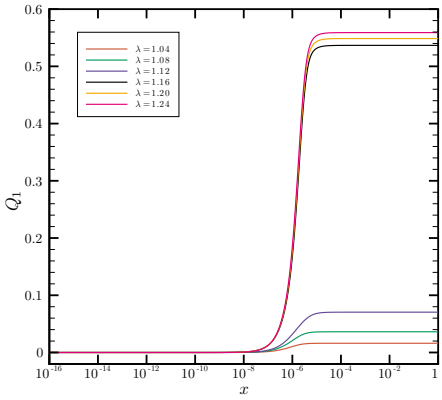

Figure 5: Plots of the asphericity Q_1 as a function of dimensionless radial position x (note logarithmic scale) for the dimensionless material parameters $\mu^* = 0.1$, $\kappa_I^* = \frac{1}{2}\kappa_{II}^* = \alpha^* = 10^{-13}$, and $q_* = 0.5$ and representative values of the degree of radial expansion λ between 1 and 1.25. Consistent with (20), note the horizontal slopes at the cylinder center ($x = 0$) and outer boundary ($x = 1$).

nature of these materials, it seems reasonable to expect that the moduli would be at least an order of magnitude greater. So, we took $\kappa_I = 10^{-11}$ J/m and $\kappa_{II} = 2 \times 10^{-11}$ J/m. The value of the splay modulus is also in line with values used in previous work.[1–3, 26]. With the expectation that the regularizing modulus should not exceed the splay modulus, we chose $\alpha = 10^{-11}$. As a result, $\mu^* = 10^{-1}$ and $\kappa_I^* = \frac{1}{2}\kappa_{II}^* = \alpha^* = 10^{-13}$. Since radial expansion ($\lambda > 1$) is expected to give rise to prolate asphericities ($q_1 > 0$ and perhaps $q_2 > 0$ as well) perpendicular to the cylinder axis, the choice $q_* > 0$ is sensible for this case. Similarly, because we expect oblate asphericities ($-1 < q_1 < 0$ and perhaps $q_2 < 0$ too) perpendicular to the axis to arise for radial contraction ($0 < \lambda < 1$), we choose $-1 < q_* < 0$ in this setting. So, for illustrative purposes, we took $q_* = 0.5$ for radial expansion and $q_* = -0.4$ for radial contraction.

With these parameters, we solved (19)–(20) from $x = 0$ to $x = 1$ using the ACDC package[27] with the tolerance on the solution pair (Q_1, Q_2) set to 10^{-8} and that of its derivative $(dQ_1/dx, dQ_2/dx)$ set to 10^{-4} for radial expansion and 10^{-3} for radial contraction. As our initial, trial solution, we used the straight line $Q_1 = Q_2 = 0$, satisfying (20) and consisting of 5001 evenly spaced points on the closed domain. The only parameter varied was λ, the degree of radial expansion or contraction. Thus, the range of λ for axial contraction; the values of μ^*, ν, κ_I^*, and α^*; and the solution method were identical to those used in our previous investigations.[1–3]

3.1 Radial expansion ($\lambda > 1$)

For the regime of radial expansion, we allowed λ to range between 1 and 1.25. Figures 5 and 6 show the solution profiles for Q_1 and Q_2 and the sharp transition between isotropic ($Q_\beta = 0$, $\beta = 1, 2$) and anisotropic ($Q_\beta \neq 0$) regions along the cylinder radius, thereby indicating the presence of a disclination of strength +1 located along the cylinder axis.

The extent of the disclination core can also be inferred from the plot as the region where Q_1 and Q_2 exhibit rapid increases.[13] Although the solutions for Q_1 and Q_2 appear identical in Figures 5 and 6, it becomes apparent in Figure 7 that they differ but only in the core region, where Q_2 exhibits an increased gradient due to the larger value of

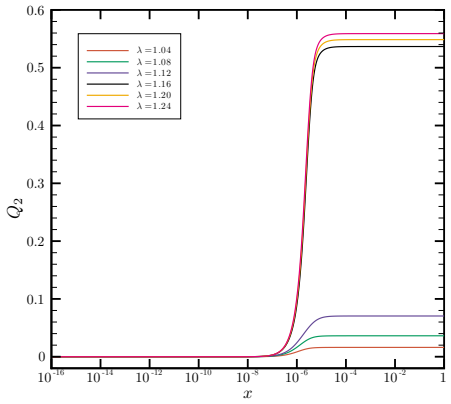

Figure 6: Plots of the asphericity Q_2 as a function of dimensionless radial position x (note logarithmic scale) for the dimensionless material parameters $\mu^* = 0.1$, $\kappa_I^* = \frac{1}{2}\kappa_{II}^* = \alpha^* = 10^{-13}$, and $q_* = 0.5$ and representative values of the degree of radial expansion λ between 1 and 1.25. Consistent with (20), note the horizontal slopes at the cylinder center ($x = 0$) and outer boundary ($x = 1$).

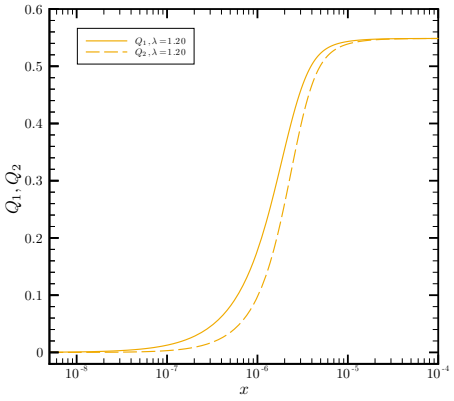

Figure 7: Plot of the asphericities Q_1 and Q_2 in the core region as a function of dimensionless radial position x (note logarithmic scale) for the degree of radial expansion $\lambda = 1.20$ and the dimensionless material parameters $\mu^* = 0.1$, $\kappa_I^* = \frac{1}{2}\kappa_{II}^* = \alpha^* = 10^{-13}$, and $q_* = 0.5$.

$\kappa_{I\!I}$ compared to κ_I.* Despite this difference, from Figures 5 and 6, the center of the transition zone for both Q_1 and Q_2 appears to be at $x = 10^{-6}$, corresponding to a dimensional core radius on the order of 10^{-2} μm and consistent with the length scale predicted by the ratios $\sqrt{\kappa_I/\mu}$ and $\sqrt{\kappa_{I\!I}/\mu}$ for our choices of μ, κ_I, and $\kappa_{I\!I}$.† Our core radius, which we denote by x_c, is also of the same order as values observed for liquid crystalline melts.[28] Since our uniaxial energy density investigations resulted in disclinations with similar characteristics,[1–3] these results are not unexpected. What is important to emphasize is that, since both Q_1 and Q_2 are nonvanishing for $x > x_c$, the states obtained here are *biaxial*.

To investigate the energetic status of these biaxial states, we introduce the dimensionless free-energy density $\Psi = \psi/\nu$. In view of the assumptions concerning the deformation $\boldsymbol{y}$, the orientations $\boldsymbol{n}_1$ and $\boldsymbol{n}_2$, and the asphericities q_1 and q_2,

$$\Psi = \frac{\psi}{\nu} = \Psi_e + \Psi_a + \Psi_o, \tag{23}$$

with

$$\Psi_e = \frac{\mu^*}{2}\Big(2\lambda^2 + \frac{1}{\lambda^4} - 3\Big) \tag{24}$$

a conventional neo-Hookean rubber-elastic contribution associated with the distortion of the network,

$$\begin{aligned}\Psi_a = \frac{\mu^*}{2}\Big(\lambda^2\Big(\frac{(1+Q_2)^{\frac{1}{3}}}{(1+Q_1)^{\frac{2}{3}}} + \frac{(1+Q_1)^{\frac{1}{3}}}{(1+Q_2)^{\frac{2}{3}}} - 2\Big) + \frac{1}{\lambda^4}\big((1+Q_1)^{\frac{1}{3}}(1+Q_2)^{\frac{1}{3}} - 1\big)\Big) \\ + \frac{\Phi(Q_1,Q_2)}{\nu} + \frac{2\delta}{\nu}Q_1(Q_1-Q_*)Q_2(Q_2-Q_*) + \frac{\alpha^*}{2}\Big(\Big(\frac{dQ_1}{dx}\Big)^2 + \Big(\frac{dQ_2}{dx}\Big)^2\Big)\end{aligned} \tag{25}$$

a contribution associated with the asphericity of the molecular conformation, and

$$\Psi_o = \frac{(\kappa_I^* + \kappa_{I\!I}^*)\lambda^2\Gamma(Q_1,Q_2)}{2x^2} \tag{26}$$

a contribution associated with the axes of the molecular conformation.

A comparision of the total neo-Hookean energy

$$\mathcal{F}_e^{\rm tot} = \int_0^1 \Psi_e(x)x\,dx, \tag{27}$$

the total energy from our previously performed uniaxial investigations $\mathcal{F}_{\rm uni}^{\rm tot}$,[1–3] and the total free-energy

$$\mathcal{F}^{\rm tot} = \int_0^1 \Psi(x)x\,dx \tag{28}$$

plotted in Figure 8 shows that the material strongly prefers a disclinated state in which the conformation of the material surrounding the core is biaxial as opposed to uniaxial. While $\mathcal{F}_e^{\rm tot}$ increases monotonically with λ, $\mathcal{F}^{\rm tot}$ is a double-well potential with an absolute minimum at $\lambda = 1$ and a relative minimum at $\lambda \approx 1.13$. Also, for all $\lambda > 1$, $\mathcal{F}^{\rm tot}$

*For clarity, Figure 7 focuses just on $\lambda = 1.20$, but similar behavior is evident for the studied range of λ.

†The ratios $\sqrt{\kappa_I/\mu}$ and $\sqrt{\kappa_{I\!I}/\mu}$ determine the length scale at which a cross-over between rubber-elastic and orientational effects occurs.[4–5,7]

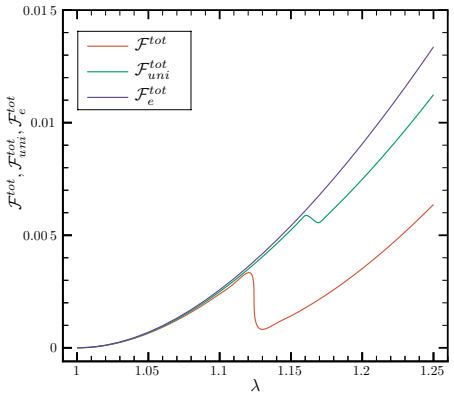

Figure 8: Plots of the total neo-Hookean rubber-elastic energy $\mathcal{F}_e^{\text{tot}}$ and of the total free-energy $\mathcal{F}^{\text{tot}}$ as a function of the degree of radial expansion λ between 1 and 1.25 for the dimensionless material parameters $\mu^* = 0.1$, $\kappa_I^* = \frac{1}{2}\kappa_{II}^* = \alpha^* = 10^{-13}$, and $q_* = 0.5$.

is less than both $\mathcal{F}_{\text{uni}}^{\text{tot}}$ and $\mathcal{F}_e^{\text{tot}}$, the isotropic ($Q_1 = Q_2 = 0$) neo-Hookean contribution alone. This difference is negligible for all $\lambda \leq 1.12$, and we therefore do not necessarily expect a disclinated state to form in the range $1 \leq \lambda < 1.12$. However, beyond $\lambda = 1.12$, the difference between $\mathcal{F}^{\text{tot}}$ and $\mathcal{F}_e^{\text{tot}}$ becomes non-trivial and shows an energetic motivation for the material to form a disclinated state in which the material outside the core boundary x_c in a biaxially anisotropic state. It is interesting to note from Figure 8 that not only is a biaxial state energetically preferred over a uniaxial one ($\mathcal{F}^{\text{tot}}$ always falls below $\mathcal{F}_{\text{uni}}^{\text{tot}}$ for our range of λ) but also that the threshold value of λ at which a biaxial disclination first manifests itself is less than that arising when the extra-core region is constrained to be uniaxial.

In addition, we investigated the total free-energy of the core, which we denote as

$$\mathcal{F}^{\text{core}} = \int_0^{x_c} \Psi(x) x \, dx, \tag{29}$$

relative to that of the whole domain. From Figure 9, it is evident that $\mathcal{F}^{\text{core}}$ is a vanishingly small percentage of $\mathcal{F}^{\text{tot}}$. This is because of the relatively small size of the core and the fact that Ψ_e is of a comparatively large magnitude across the entire radial extent of the cylinder. As in our previous studies,[1–3] the proportion of total free-energy contained in the core remains relatively constant up to the value of λ corresponding to the first inflection point of $\mathcal{F}^{\text{tot}}$. Coincident with the threshold value of λ seen in Figure 8, a sharp increase then occurs, and the proportion then decreases monotonically for the remainder of our range as more energy goes into both stretching of the polymer network and changing the conformation of the chains comprising the network.

The dimensionless pressure P given in (17) is shown in Figure 10. Because the material becomes biaxial with $Q_1 \neq 0$ and $Q_2 \neq 0$, the pressure differs both in magnitude and character from that arising in the uniaxial case.[1–3] $Q_1 = Q_2$ except for the transition layer, the term $I_1(x)$ in (17) vanishes everywhere but within the layer. In the isotropic core, where $Q_1 = Q_2 = 0$, the pressure coincides with its neo-Hookean counterpart and is an order of magnitude lower than in the uniaxial case.[1–3] Outside the core, with the increase in both Q_1 and Q_2 shown in Figures 5 and 6, the pressure drops below the neo-Hookean value. Recall that, for an incompressible material, the pressure is a reaction which arises in response to the constraint $\det \boldsymbol{F} = 1$. The excessive core pressure found in the uniaxial case, which general exceeds its biaxial counterpart by an order of magnitude, indicates that the material is overly constrained when it is forced to remain incompressible

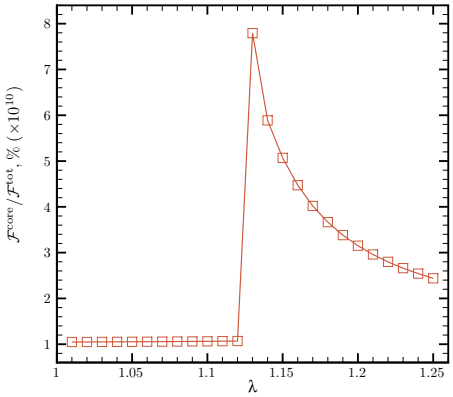

Figure 9: Plot of the percentage $\mathcal{F}^{\rm core}/\mathcal{F}^{\rm tot}$ of free energy in the core as a function of the degree of cylinder distortion λ between 1 and 1.25 for the dimensionless material parameters $\mu^* = 0.1$, $\kappa_I^* = \frac{1}{2}\kappa_{II}^* = \alpha^* = 10^{-13}$, $q_* = 0.5$, and $\delta = 0$.

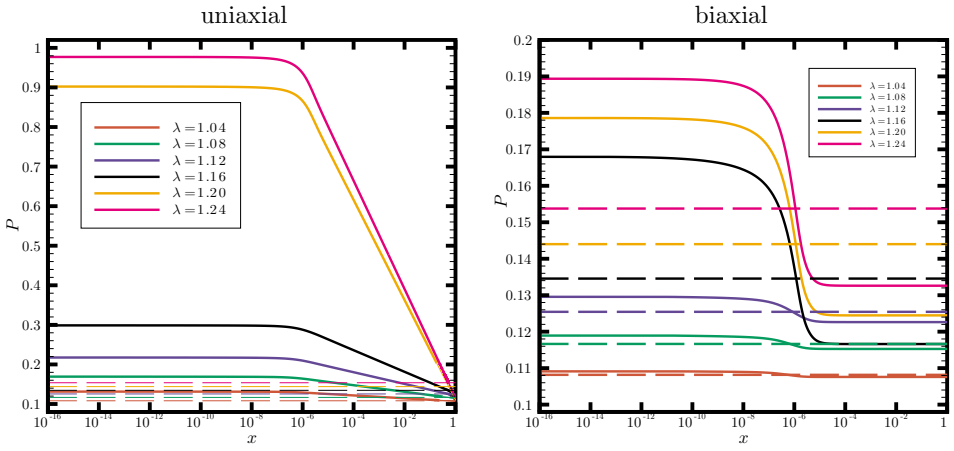

Figure 10: Plot of the dimensionless pressure P for the uniaxial case[2] and the present biaxial case as a function of dimensionless radial position x (note logarithmic scale) for the dimensionless material parameters $\mu^* = 0.1$, $\kappa_I^* = \frac{1}{2}\kappa_{II}^* = \alpha^* = 10^{-13}$, $q_* = 0.5$, and $\delta = 0$ and representative values of the degree of radial expansion λ between 1 and 1.25. Dashed lines show corresponding neo-Hookean values of P.

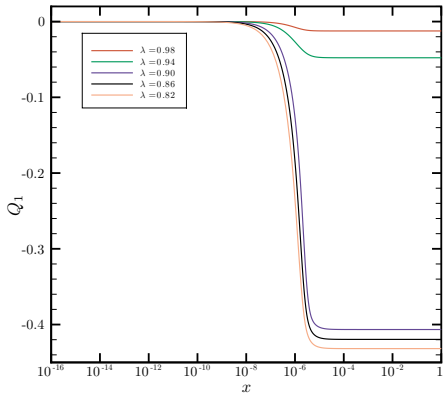

Figure 11: Plots of the asphericity Q_1 as a function of dimensionless radial position x (note logarithmic scale) for the dimensionless material parameters $\mu^* = 0.1$, $\kappa_I^* = \frac{1}{2}\kappa_{II}^* = \alpha^* = 10^{-13}$, and $q_* = -0.4$ and representative values of the degree of axial expansion λ between 1 and 0.80. Consistent with (20), note the horizontal slopes at the cylinder center ($x = 0$) and outer boundary ($x = 1$).

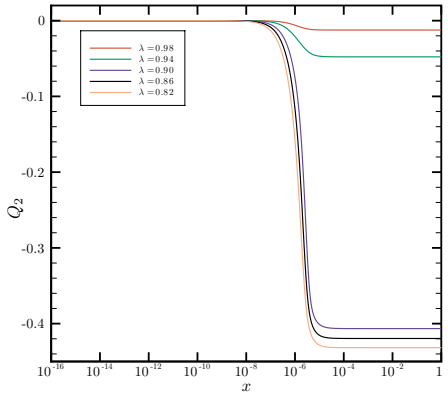

Figure 12: Plots of the asphericity Q_2 as a function of dimensionless radial position x (note logarithmic scale) for the dimensionless material parameters $\mu^* = 0.1$, $\kappa_I^* = \frac{1}{2}\kappa_{II}^* = \alpha^* = 10^{-13}$, and $q_* = -0.4$ and representative values of the degree of axial expansion λ between 1 and 0.80. Consistent with (20), note the horizontal slopes at the cylinder center ($x = 0$) and outer boundary ($x = 1$).

and biaxial conformations are disallowed. When biaxial conformations are allowed, there is a concomitant decrease in the reactive pressure and that decrease further confirms the preference of the material for a biaxial state.

3.2 Radial contraction $(0 < \lambda < 1)$

The analogous problem of axial extension was investigated with a range of λ between 1 and 0.80. As in the case of axial contraction, plots of the asphericities Q_1 and Q_2 shown in Figures 11 and 12 show the sharp transition between isotropic ($Q_1 = Q_2 = 0$) and anisotropic ($Q_1 = Q_2 \neq 0$) regions along the cylinder radius, consistent with the presence of a biaxial disclination of strength +1 located along the cylinder axis. As in the case of axial contraction, the asphericities Q_1 and Q_2 are equal except in the core region (see Figure 13 where Q_2 exhibits a steeper gradient due to the larger value of κ_{II} compared

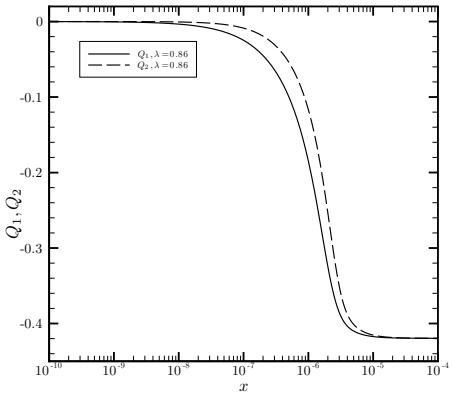

Figure 13: Plot of the asphericities Q_1 and Q_2 in the core region as a function of dimensionless radial position x (note logarithmic scale) for the degree of axial expansion $\lambda = 0.86$ and the dimensionless material parameters $\mu^* = 0.1$, $\kappa_I^* = \frac{1}{2}\kappa_{II}^* = \alpha^* = 10^{-13}$, and $q_* = -0.4$.

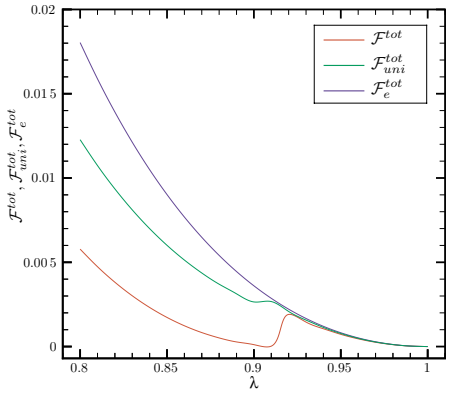

Figure 14: Plots of the total neo-Hookean rubber-elastic energy $\mathcal{F}_e^{\rm tot}$ and of the total free-energy $\mathcal{F}^{\rm tot}$ as a function of the degree of axial expansion λ between 1 and 0.80 for the dimensionless material parameters $\mu^* = 0.1$, $\kappa_I^* = \frac{1}{2}\kappa_{II}^* = \alpha^* = 10^{-13}$, and $q_* = -0.4$.

to κ_I). Nevertheless, from Figures 11 and 12, the center of the transition zone for both Q_1 and Q_2 appears to be at $x = 10^{-6}$, corresponding to a dimensional core radius on the order of 10^{-2} μm.

The energies $\mathcal{F}_e^{\rm tot}$, $\mathcal{F}_{\rm uni}^{\rm tot}$, $\mathcal{F}^{\rm tot}$ for radial contraction are plotted in Figure 14. Here too, as for radial expansion, there is an energetic motivation for the material to achieve a biaxial disclinated state, especially for $\lambda < 0.92$. This threshold value of λ occurs sooner; i.e., at a lesser degree of radial contraction, than for the corresponding uniaxial case.

The behavior of the total free-energy $\mathcal{F}^{\rm core}$ of the core is similar to that observed for axial contraction. The proportion of total free-energy contained in the core remains relatively constant up to the value of λ corresponding to the first inflection point of $\mathcal{F}^{\rm tot}$. As before, coincident with the threshold value of λ of the total free-energy in Figure 14, a sharp increase then occurs, and the proportion then decreases monotonically for the rest of the range.

As in the case of radial expansion, a determination of the pressure from (17) can be made. These results are omitted here for brevity.

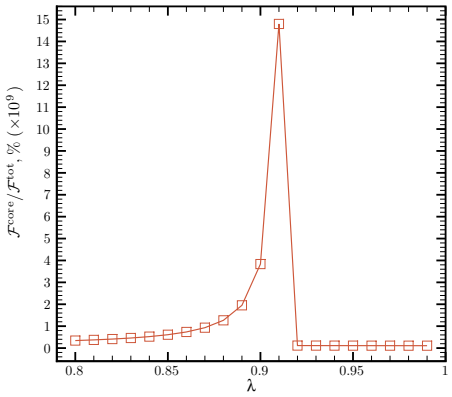

Figure 15: Plot of the percentage $\mathcal{F}^{\rm core}/\mathcal{F}^{\rm tot}$ of free energy in the core as a function of the degree of cylinder distortion λ between 1 and 0.80 for the dimensionless material parameters $\mu^* = 0.1$, $\kappa_I^* = \frac{1}{2}\kappa_{I\!I}^* = \alpha^* = 10^{-13}$, $q_* = -0.4$, and $\delta = 0$.

4 Bifurcation and stability

A priori, the uniqueness and stability of the numerical solutions discussed in Section 3 are unclear. To address these issues, we examine the solution set for the boundary-value problem (19)–(20) for scalings where κ_I^*, $\kappa_{I\!I}^*$, and α^* are all very small in comparison to μ^*. Considering the structure of (19) and the numerical results depicted in Figures 5, 6, 11, and 12, we find that for each $\lambda \neq 1$, the profiles of the solution pair (Q_1, Q_2) exhibit three well-defined regions:

- a core region surrounding the cylinder axis where (Q_1, Q_2) is uniform and very close to zero;
- an extra-core region within which (Q_1, Q_2) is uniform but nonvanishing;
- a transition layer connecting the core and extra-core regions.

Granted the scaling considered here, the dimensionless core region is both very thin, with width on the order of 10^{-6} (Figures 7 and 13), and energetically insignificant since its share of the free-energy is never more than a minute percentage of the total (Figures 9 and 15). The structure of the transition layer is the same for all relevant λ; it monotonically connects $Q_1 = Q_2 = 0$ at $x = 0$ to the value of $Q_1 = Q_2 \neq 0$ in the extra-core region. We thus focus on the extra-core regime where symmetric behavior prevails in the sense that $Q_1 = Q_2 = Q$. A breakdown of this symmetry occurs only when the full domain is taken into account as in the previous section (Figures 5 and 6). Neglecting the small parameters α^*, κ_I^*, and $\kappa_{I\!I}^*$ associated with the core boundary, we specialize (19) to the extra-core region. This yields the algebraic equation,

$$f(Q,\lambda) = \frac{\mu^*\lambda^2}{6(1+Q)^{\frac{1}{3}}}\Big(-\frac{1}{1+Q}+\frac{1}{\lambda^6}\Big) + \frac{Q(Q-Q_*)(Q^2+2Q-Q_*)}{(1+Q)^3} = 0, \qquad (30)$$

that should provide the uniform, common value Q of Q_1 and Q_2 outside the core. To predict the response of the material to any particular choice of λ, we would like to solve (30) for Q as a function of λ. Unfortunately, (30) contains fractional powers of Q and doesn't easily lend itself to direct analytical solution. To circumvent this obstacle, we note that (30) can be expressed as a cubic for λ^2, viz.,

$$\lambda^6 + 3b\lambda^4 + c = 0,$$

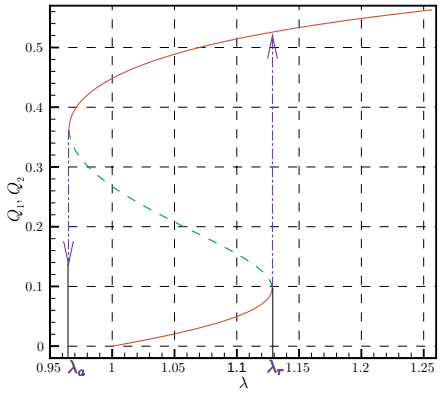

Figure 16: Plot of the constant, 'bulk' asphericity Q as a function of the degree of radial expansion λ between 1 and 1.25 for the dimensionless material parameters $\mu^* = 0.1$ and $q_* = 0.5$. The equilibrium set consists of two (lower and upper) stable branches, and one (middle) unstable branch. When a certain deformation of $\lambda_r \approx 1.13$ is reached, the solution switches from the lower to the upper branch, with a sharp increase in Q (cf. Figures 5 and 6). A classical hysteresis loop is present.

where

$$b = -\frac{2Q(Q-Q_*)(Q^2+2Q-Q_*)}{\mu^*(1+Q)^{\frac{5}{3}}} \qquad \text{and} \qquad c = -(1+Q).$$

Solving this equation yields

$$\lambda = \sqrt{b + s_-(b,c) + s_+(b,c)},$$

with

$$s_\pm(b,c) = -\left(\frac{b^2}{3} + \frac{c}{2} \pm \sqrt{\frac{b^3 c}{3} + \frac{c^2}{4}}\right)^{\frac{1}{3}}.$$

A real value of λ is guaranteed by the range of parameters under consideration.

Having obtained $\lambda = \lambda(Q)$, we now turn to finding the originally desired function $Q = Q(\lambda)$ by plotting bifurcation diagrams for (30). The case of radial expansion ($\lambda > 1$) is shown in Figure 16 while that of radial contaction ($\lambda < 1$) appears in Figure 17. This provides substantial insight into the results obtained by direct numerical solution of the governing boundary-value problem (19)–(20) and shown in Figures 5, 6, 11, and 12. For axial contraction, we start from the point $(\lambda, Q) = (1, 0)$ in Figure 16, slowly increase the value of λ, and follow the lower branch of the diagram up to $\lambda = \lambda_r$. Above λ_r, the equilibrium solution for Q_1 and Q_2 is forced to switch to the upper branch (Figures 5 and 6). If we instead start on the upper branch at $\lambda > \lambda_r$ and quasi-statically release the cylinder (decrease λ), we follow the upper branch past λ_r all the way down to a point of downward snapping, where $\lambda = \lambda_a < \lambda_r$. For this to occur, we must actually contact the specimen radially since $\lambda_a \leq 1$. Therefore, classical hysteretic behavior is observed.

Similarly, for axial extension, we begin at the point $(\lambda, Q) = (1, 0)$ in Figure 17, slowly decrease the value of λ, and follow the upper branch of the diagram down to $\lambda = \lambda_r$. Below λ_r, the equilibrium solution for Q_1 and Q_2 is forced to switch to the lower branch (Figures 11 and 12). Conversely, if we start on the lower branch at $\lambda < \lambda_r$ and quasi-statically release the cylinder (increase λ), we follow the lower branch past λ_r all the way up to a point of upward snapping, where $\lambda = \lambda_a > \lambda_r$. For this to occur, the

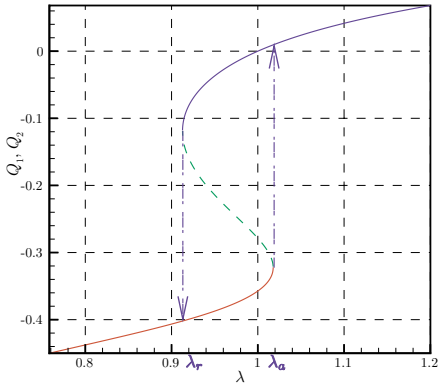

Figure 17: Plot of the constant, 'bulk' asphericity Q as a function of the degree of axial extension λ between 1 and 0.80 for the dimensionless material parameters $\mu^* = 0.1$ and $q_* = -0.4$. The equilibrium set consists of two (lower and upper) stable branches, and one (middle) unstable branch. When a certain deformation of $\lambda_r \approx 0.92$ is reached, the solution switches from the upper to the lower branch, with a sharp decrease in Q (cf. Figures 11 and 12). A classical hysteresis loop is present.

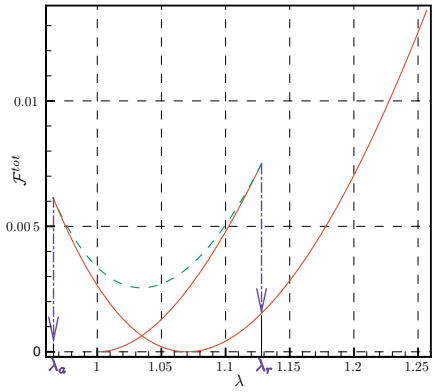

Figure 18: Plot of the total free energy of the constant, 'bulk' asphericity Q as a function of the degree of radial expansion λ between 1 and 1.25 for the dimensionless material parameters $\mu^* = 0.1$ and $q_* = 0.5$ (cf. Fig. 16). We observe two, stable (solid) branches connected by an unstable (dashed) one. Corresponding branch switching is highlighted by arrows and always leads to a lowering of the total free energy.

specimen must be contracted axially since $\lambda_a \geq 1$. Again, classical hysteretic behavior is observed.

To further clarify properties of the system, we can investigate the stability of solutions using the information about their behavior in the extra-core region obtained above. Since the bifurcation behavior observed in Figures 18 and 19 is classical, the branch stability is as shown. In the same vein, we plot the energy of the constant, bulk solution for axial contraction in Figure 18 and that for axial extension in Figure 19. We note that the sharp changes in energy shown in Figures 8 and 9 for axial contraction and Figures 14 and 15 for axial extension mirror the branch stability switching phenomenon described above. As can be seen, switching leads to a lower energy level, and thus is energetically preferable.

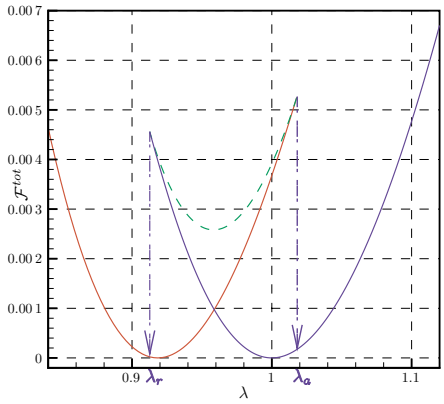

Figure 19: Plot of the total free energy of the constant, 'bulk' asphericity Q as a function of the degree of radial expansion λ between 1 and 0.80 for the dimensionless material parameters $\mu^* = 0.1$ and $q_* = -0.4$ (cf. Fig. 16). We observe two, stable (solid) branches connected by an unstable (dashed) one. Corresponding branch switching is highlighted by arrows and always leads to a lowering of the total free energy.

To determine the values of λ_r and λ_a in Figures 16 and 17, we first note from (30) that $f(Q,\lambda) = 0$ everywhere on both curves. Thus,

$$\frac{df}{dQ} = \frac{\partial f}{\partial Q} + \frac{\partial f}{\partial \lambda}\frac{\partial \lambda}{\partial Q} = 0.$$

For λ_r and λ_a, this is supplemented by the fact that $\partial\lambda/\partial Q = 0$. If $\partial f/\partial\lambda \neq 0$, then for the above equation to hold, $\partial f/\partial Q = 0$. Therefore, λ_r and λ_a can be found by solving the system $(f(Q,\lambda), \partial f(Q,\lambda)/\partial Q) = (0,0)$. This gives rise to

$$8(-2Q^2(9+Q(7+2Q))+Q(18+Q(3+Q))Q_*+(-3+5Q)Q_*^2)^2(7Q^4-4Q^3(-5+Q_*)+3Q_*^2 - 2QQ_*(9+Q_*) - 6Q^2(-3+2Q_*)) + (1+Q)^6(\mu^*)^3 = 0. \quad (31)$$

and

$$\lambda^2 = -\frac{2(18Q^2+12Q^3+3Q^4+Q(Q-Q_*)(Q(2+Q)-Q_*)+3Q_*^2-6QQ_*(3+Q_*))}{(1+Q)^{\frac{5}{3}}\mu^*} \quad (32)$$

Real solutions to (31) and (32) are not guaranteed and depend on the values of the parameters μ^* and Q_*. For the case of radial expansion studied in Section 3, $(Q,\lambda_r) = (0.097, 1.13)$ and $(Q,\lambda_a) = (0.36, 0.97)$, while for radial contraction, $(Q,\lambda_r) = (-0.12, 0.91)$ and $(Q,\lambda_a) = (-0.32, 1.02)$. These two values of λ_r respectively correspond to the point at which jumps are observed in Figures 8 and 9 for radial expansion and Figures 14 and 15 for radial contraction. If a nematic-elastomeric specimen is being prepared for an experiment, (31) and (32) can be solved with the particular μ^* and Q_* being considered to see whether real λ_a and λ_r exist and what their values are. This then gives the experimentalist an idea of the range of axial contraction or extension to investigate.

The stability analysis described above is predicated on neglecting the parameters α^*, κ_I^*, and κ_{II}^* associated with the core boundary in (19) and which are small relative to μ^*. The question therefore arises as to how small α^*, κ_I^*, and κ_{II}^* must be to safely ignore them in the extra-core region. Thus, for a given λ, below a certain threshold and regardless of their values, α^*, κ_I^*, and κ_{II}^* should affect only the core boundary region of

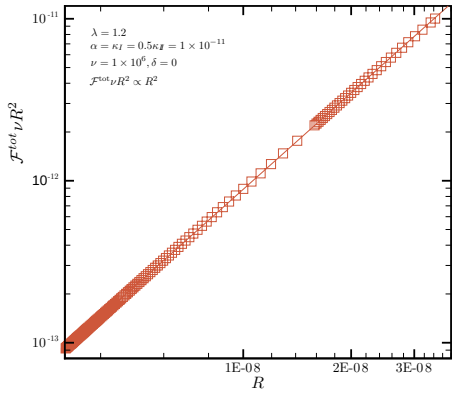

Figure 20: Plot of the dimensional total free-energy $\mathcal{F}^{\text{tot}}\nu R^2$ for the dimensionless material parameters $\mu^* = 0.1$ and $q_* = 0.5$. R ranges from 3.18×10^{-9} m to 3.43×10^{-8} m with a corresponding range of α^* of 0.99 to 0.0085.

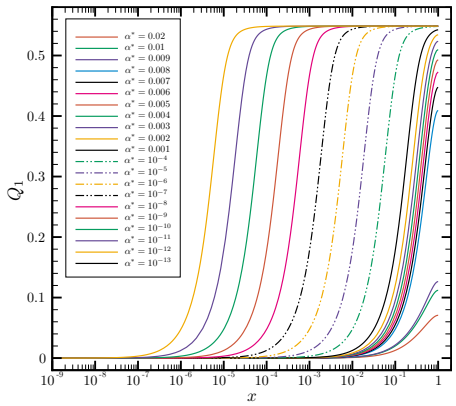

Figure 21: Plots of the asphericity Q_1 as a function of dimensionless radial position x (note logarithmic scale) for $\lambda = 1.20$ and the dimensionless material parameters $\mu^* = 0.1$ and $q_* = 0.5$. R ranges from 2.24×10^{-8} m to 1 cm with a corresponding range of α^* of 0.02 to 1×10^{-13}. Consistent with (20), note the horizontal slopes at the cylinder center ($x = 0$) and outer boundary ($x = 1$).

the solution (Q_1,Q_2) with the extra-core and core regions maintaining constant values. Keeping μ^* constant while changing the other parameters requires changing the specimen radius R. So, if the small parameters are below the threshold for constant (Q_1, Q_2), and since $\Psi = \Psi(Q_1, Q_2)$ (cf. (23)–(26)), it follows that the total, dimensional energy $\mathcal{F}^{\text{tot}}\nu R^2$ (cf. (28)) will grow as R^2.

For a representative value of $\lambda = 1.20$, we conducted a parametric study wherein $\mu = 10^5$ J/m^3, $\nu = 10^6$ J/m^3, $q_* = 0.5$, $\kappa_I = 10^{-11}$ J/m and $\kappa_{II}^* = 2 \times 10^{-11}$ J/m were kept constant as before and only R was varied from 3.18×10^{-9} m to 1 cm. As a result, $\mu^* = 10^{-1}$ remained constant, and $\kappa_I^* = \frac{1}{2}\kappa_{II}^* = \alpha^*$ varied with R from 0.99 to 1×10^{-13}. In Figure 20, $R \leq 3.43 \times 10^{-8}$ m and $\mathcal{F}^{\text{tot}}\nu R^2 \propto R^2$. This is because the solution Q_1 and Q_2 lie below the threshold for a disclination to necessarily appear as can be seen in the curves for $\alpha^* > 0.008$ in Figures 21 and 22.

For $R \geq 3.54 \times 10^{-8}$ m ($\alpha^* \leq 0.008$), a disclination is present, but for $R < 3.16 \times 10^{-7}$ m ($\alpha^* > 1 \times 10^{-4}$), the growth of $\mathcal{F}^{\text{tot}}\nu R^2 \propto R^{1.6}$ as shown in Figure 23. Since $\mathcal{F}^{\text{tot}}\nu R^2$ grows less than quadratically in this region, we expect that a disclination will be

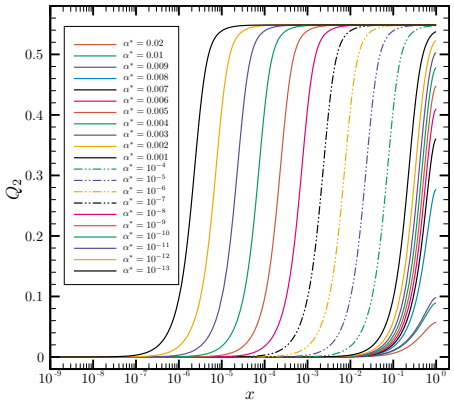

Figure 22: Plots of the asphericity Q_2 as a function of dimensionless radial position x (note logarithmic scale) for $\lambda = 1.20$ and the dimensionless material parameters $\mu^* = 0.1$ and $q_* = 0.5$. R ranges from 2.24×10^{-8} m to 1 cm with a corresponding range of α^* of 0.02 to 1×10^{-13}. Consistent with (20), note the horizontal slopes at the cylinder center ($x = 0$) and outer boundary ($x = 1$).

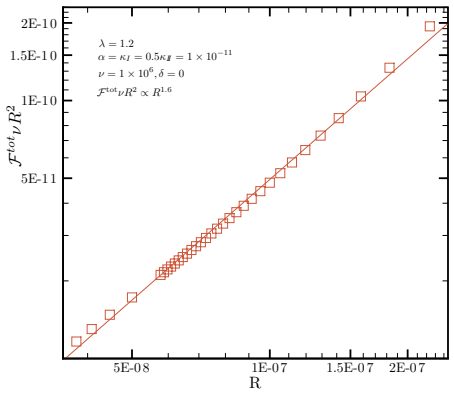

Figure 23: Plot of the total free-energy $\mathcal{F}^{\text{tot}}$ for the dimensionless material parameters $\mu^* = 0.1$ and $q_* = 0.5$. R ranges from 3.54×10^{-8} m to 2.24×10^{-7} m with a corresponding range of α^* of 0.008 to 2×10^{-4}.

easier to generate in specimens with $3.54 \times 10^{-8} \leq R < 3.16 \times 10^{-7}$ m. The growth is not quadratic because Q_1 and Q_2 in Figures 21 and 22 have not yet reached a constant extra-core value. As stated previously, once this constant value threshold has been attained for $R \geq 3.16 \times 10^{-7}$ m ($\alpha^* \leq 1 \times 10^{-4}$), the small parameters only have an effect in the boundary layer. Thus, as shown in Figure 24, if $R \geq 3.16 \times 10^{-7}$ m ($\alpha^* \leq 1 \times 10^{-4}$), $\mathcal{F}^{\text{tot}}\nu R^2 \propto R^2$, and we see that the small parameters can only be discarded for this regime.

5 Discussion

We have extended a previously studied to allow for biaxiality of the molecular conformation. In so doing, we have found that nematic elastomers can sustain disclinations with an isotropic core and an extra-core region in which the conformation is biaxial rather than uniaxial. These states possess lower energies than the corresponding ones for materials

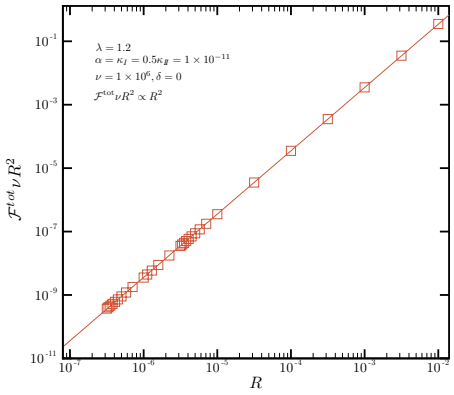

Figure 24: Plot of the total free-energy $\mathcal{F}^{\text{tot}}$ for the dimensionless material parameters $\mu^* = 0.1$ and $q_* = 0.5$. R ranges from 3.16×10^{-7} m to 1 cm with a corresponding range of α^* of 1×10^{-4} to 1×10^{-13}.

whose conformations are constrained to remain uniaxial. Furthermore, when compared to both the uniaxial and neo-Hookean cases, the reactive pressure required to maintain the constraint of material incompressibility within the disclination core is reduced by an order of magnitude. Thus, a biaxial disclinated state is a more natural one for the material to inhabit. In addition, we have used bifurcation and stability analyses to expand our insight regarding the properties of the governing equations and confidence into the numerical results. These analyses include the derivation of analytic expressions for the threshold values of radial expansion and contraction at which a biaxial disclinated state clearly becomes energetically preferred and a determination of the stability of solutions for the studied parameter values. Finally, for a representative case of axial contraction, we find the threshold at which the small parameters only affect the core boundary region and thus cause the total dimensional energy to vary with R^2 as theoretically predicted. When the parameters exceed the threshold, the dimensional energy varies as $R^{1.6}$, and we infer that a disclination will form more easily in specimens in this regime.

Acknowledgments

We thank Don Carlson for many valuable discussions. This work was supported by the National Science Foundation and the Department of Energy.

References

1. Fried, E.; Todres, R.E. *Proc Natl Acad Sci USA* 2001, 98, 14773–14777.
2. Fried, E.; Todres, R.E. *J Mech Phys Solids* 2002, 50, 2691-2716.
3. Fried, E.; Todres, R.E. *J Polym Sci Part B: Polym Phys* 2002, 40, 2098-2106.
4. Verwey, G.C.; Warner, M.; Terentjev, E.M. *J Phys II* 1996, 6, 1273–1290.
5. Finkelmann, H.; Kundler, I.; Terentjev, E.M.; Warner, M. *J Phys II* 1997, 7, 1059–1069.
6. Conti, S.; DeSimone, A.; Dolzmann, G. *J Mech Phys Solids* 2002, 50, 1431–1451.
7. Fried, E.; Korchagin, V. Int *J Solids Struct* 2002, 39, 3451–3467.
8. Kléman, M. *Rep Prog Phys* 1989, 52, 555–654.
9. Mottram, N.J.; Sluckin, T.J. *Liq Cryst* 2000, 27, 1301–1304.
10. Jones, J.C.; Graham, A.; Bryan-Brown, G.P.; Wood, E.P.; Brett, P. 2000 Proceedings of ASET International Forum on Low Power Displays, Tokyo, 17–24.
11. Chandrasekhar, S. *Contemp Phys* 1988, 29, 527–558.
12. Adrienko, D.; Allen, M.P. *Phys Rev E* 61, 504–510.
13. Mottram, N.J.; Hogan, S.J. *Philos Trans R Soc London*, Ser A 1997, 355, 2045–2064.
14. Oseen, W.C. *Trans Faraday Soc* 1933, 29, 883–899.
15. Zöcher, H. *Trans Faraday Soc* 1933, 29, 945–957.
16. Frank, F.C. *Discuss Faraday Soc* 1958, 250, 19–28.

17. Ericksen, J.L. *Arch Rational Mech Anal* 1991, 113, 97–120.
18. Cladis, P.E.; Kléman, M. *J Phys* 1972, 33, 591–598.
19. Meyer, R.B. *Phil Mag* 1973, 27, 405–424.
20. Williams, C.; Pierański, P.; Cladis, P.E. *Phys Rev Lett* 1972, 29, 90–92.
21. Warner, M.; Gelling, K.P.; Vilgis, T.A. *J Chem Phys* 1988, 88, 4008–4013.
22. Haller, I. *J Chem Phys* 1972, 57, 1400–1405.
23. Bunning, J.D.; Faber, T.E.; Sherell, P.L. *J Physique*, 1981, 42, 1175–1182.
24. Bradshaw, M.J., Raynes, E.P. *J Physique*, 1985, 46, 1513-1520.
25. Virga, E.G. *Variational Theories for Liquid Crystals*, 1994, Chapman & Hall, London.
26. Warner, M.; Terentjev, E.M. *Prog Polym Sci* 1996, 21, 853–891.
27. Cash, J.R.; Wright, R.W. *Appl Numer Math* 1988, 28, 227–244.
28. Chandrasekhar, S.; Ranganath, G.S. *Adv Phys* 1986, 35, 507–596.

List of Recent TAM Reports

No.	Authors	Title	Date
944	Wang, J., N. R. Sottos, and R. L. Weaver	Laser induced thin film spallation—*Experimental Mechanics* (submitted)	May 2000
945	Riahi, D. N.	Magnetohydrodynamic effects in high gravity convection during alloy solidification—In *Centrifugal Materials Processing* (L. L. Regel and W. R. Wilcox, eds.), 317–324 (2001)	June 2000
946	Gioia, G., Y. Wang, and A. M. Cuitiño	The energetics of heterogeneous deformation in open-cell solid foams—*Proceedings of the Royal Society of London A* **457**, 1079–1096 (2001)	June 2000
947	Kessler, M. R., and S. R. White	Self-activated healing of delamination damage in woven composites—*Composites A: Applied Science and Manufacturing* **32**, 683–699 (2001)	June 2000
948	Phillips, W. R. C.	On the pseudomomentum and generalized Stokes drift in a spectrum of rotational waves—*Journal of Fluid Mechanics* **430**, 209–229 (2001)	July 2000
949	Hsui, A. T., and D. N. Riahi	Does the Earth's nonuniform gravitational field affect its mantle convection?—*Physics of the Earth and Planetary Interiors* (submitted)	July 2000
950	Phillips, J. W.	Abstract Book, 20th International Congress of Theoretical and Applied Mechanics (27 August – 2 September, 2000, Chicago)	July 2000
951	Vainchtein, D. L., and H. Aref	Morphological transition in compressible foam—*Physics of Fluids* **13**, 2152–2160 (2001)	July 2000
952	Chaïeb, S., E. Sato-Matsuo, and T. Tanaka	Shrinking-induced instabilities in gels	July 2000
953	Riahi, D. N., and A. T. Hsui	A theoretical investigation of high Rayleigh number convection in a nonuniform gravitational field—*International Journal of Pure and Applied Mathematics*, in press (2003)	Aug. 2000
954	Riahi, D. N.	Effects of centrifugal and Coriolis forces on a hydromagnetic chimney convection in a mushy layer—*Journal of Crystal Growth* **226**, 393–405 (2001)	Aug. 2000
955	Fried, E.	An elementary molecular-statistical basis for the Mooney and Rivlin–Saunders theories of rubber-elasticity—*Journal of the Mechanics and Physics of Solids* **50**, 571–582 (2002)	Sept. 2000
956	Phillips, W. R. C.	On an instability to Langmuir circulations and the role of Prandtl and Richardson numbers—*Journal of Fluid Mechanics* **442**, 335–358 (2001)	Sept. 2000
957	Chaïeb, S., and J. Sutin	Growth of myelin figures made of water soluble surfactant—Proceedings of the 1st Annual International IEEE–EMBS Conference on Microtechnologies in Medicine and Biology (October 2000, Lyon, France), 345–348	Oct. 2000
958	Christensen, K. T., and R. J. Adrian	Statistical evidence of hairpin vortex packets in wall turbulence—*Journal of Fluid Mechanics* **431**, 433–443 (2001)	Oct. 2000
959	Kuznetsov, I. R., and D. S. Stewart	Modeling the thermal expansion boundary layer during the combustion of energetic materials—*Combustion and Flame*, in press (2001)	Oct. 2000
960	Zhang, S., K. J. Hsia, and A. J. Pearlstein	Potential flow model of cavitation-induced interfacial fracture in a confined ductile layer—*Journal of the Mechanics and Physics of Solids*, **50**, 549–569 (2002)	Nov. 2000
961	Sharp, K. V., R. J. Adrian, J. G. Santiago, and J. I. Molho	Liquid flows in microchannels—Chapter 6 of *CRC Handbook of MEMS* (M. Gad-el-Hak, ed.) (2001)	Nov. 2000
962	Harris, J. G.	Rayleigh wave propagation in curved waveguides—*Wave Motion* **36**, 425–441 (2002)	Jan. 2001
963	Dong, F., A. T. Hsui, and D. N. Riahi	A stability analysis and some numerical computations for thermal convection with a variable buoyancy factor—*Journal of Theoretical and Applied Mechanics* **2**, 19–46 (2002)	Jan. 2001

List of Recent TAM Reports (cont'd)

No.	*Authors*	*Title*	*Date*
964	Phillips, W. R. C.	Langmuir circulations beneath growing or decaying surface waves—*Journal of Fluid Mechanics* (submitted)	Jan. 2001
965	Bdzil, J. B., D. S. Stewart, and T. L. Jackson	Program burn algorithms based on detonation shock dynamics—*Journal of Computational Physics* (submitted)	Jan. 2001
966	Bagchi, P., and S. Balachandar	Linearly varying ambient flow past a sphere at finite Reynolds number: Part 2—Equation of motion—*Journal of Fluid Mechanics* (submitted)	Feb. 2001
967	Cermelli, P., and E. Fried	The evolution equation for a disclination in a nematic fluid—*Proceedings of the Royal Society A* **458**, 1–20 (2002)	Apr. 2001
968	Riahi, D. N.	Effects of rotation on convection in a porous layer during alloy solidification—Chapter 12 in *Transport Phenomena in Porous Media* (D. B. Ingham and I. Pop, eds.), 316–340 (2002)	Apr. 2001
969	Damljanovic, V., and R. L. Weaver	Elastic waves in cylindrical waveguides of arbitrary cross section—*Journal of Sound and Vibration* (submitted)	May 2001
970	Gioia, G., and A. M. Cuitiño	Two-phase densification of cohesive granular aggregates—*Physical Review Letters* **88**, 204302 (2002) (in extended form and with added co-authors S. Zheng and T. Uribe)	May 2001
971	Subramanian, S. J., and P. Sofronis	Calculation of a constitutive potential for isostatic powder compaction—*International Journal of Mechanical Sciences* (submitted)	June 2001
972	Sofronis, P., and I. M. Robertson	Atomistic scale experimental observations and micromechanical/continuum models for the effect of hydrogen on the mechanical behavior of metals—*Philosophical Magazine* (submitted)	June 2001
973	Pushkin, D. O., and H. Aref	Self-similarity theory of stationary coagulation—*Physics of Fluids* **14**, 694–703 (2002)	July 2001
974	Lian, L., and N. R. Sottos	Stress effects in ferroelectric thin films—*Journal of the Mechanics and Physics of Solids* (submitted)	Aug. 2001
975	Fried, E., and R. E. Todres	Prediction of disclinations in nematic elastomers—*Proceedings of the National Academy of Sciences* **98**, 14773–14777 (2001)	Aug. 2001
976	Fried, E., and V. A. Korchagin	Striping of nematic elastomers—*International Journal of Solids and Structures* **39**, 3451–3467 (2002)	Aug. 2001
977	Riahi, D. N.	On nonlinear convection in mushy layers: Part I. Oscillatory modes of convection—*Journal of Fluid Mechanics* **467**, 331–359 (2002)	Sept. 2001
978	Sofronis, P., I. M. Robertson, Y. Liang, D. F. Teter, and N. Aravas	Recent advances in the study of hydrogen embrittlement at the University of Illinois—Invited paper, Hydrogen–Corrosion Deformation Interactions (Sept. 16–21, 2001, Jackson Lake Lodge, Wyo.)	Sept. 2001
979	Fried, E., M. E. Gurtin, and K. Hutter	A void-based description of compaction and segregation in flowing granular materials—*Proceedings of the Royal Society of London A* (submitted)	Sept. 2001
980	Adrian, R. J., S. Balachandar, and Z.-C. Liu	Spanwise growth of vortex structure in wall turbulence—*Korean Society of Mechanical Engineers International Journal* **15**, 1741–1749 (2001)	Sept. 2001
981	Adrian, R. J.	Information and the study of turbulence and complex flow—*Japanese Society of Mechanical Engineers Journal B*, in press (2002)	Oct. 2001
982	Adrian, R. J., and Z.-C. Liu	Observation of vortex packets in direct numerical simulation of fully turbulent channel flow—*Journal of Visualization*, in press (2002)	Oct. 2001
983	Fried, E., and R. E. Todres	Disclinated states in nematic elastomers—*Journal of the Mechanics and Physics of Solids* **50**, 2691–2716 (2002)	Oct. 2001
984	Stewart, D. S.	Towards the miniaturization of explosive technology—Proceedings of the 23rd International Conference on Shock Waves (2001)	Oct. 2001
985	Kasimov, A. R., and Stewart, D. S.	Spinning instability of gaseous detonations—*Journal of Fluid Mechanics* (submitted)	Oct. 2001
986	Brown, E. N., N. R. Sottos, and S. R. White	Fracture testing of a self-healing polymer composite—*Experimental Mechanics* (submitted)	Nov. 2001

List of Recent TAM Reports (cont'd)

No.	*Authors*	*Title*	*Date*
987	Phillips, W. R. C.	Langmuir circulations—*Surface Waves* (J. C. R. Hunt and S. Sajjadi, eds.), in press (2002)	Nov. 2001
988	Gioia, G., and F. A. Bombardelli	Scaling and similarity in rough channel flows—*Physical Review Letters* **88**, 014501 (2002)	Nov. 2001
989	Riahi, D. N.	On stationary and oscillatory modes of flow instabilities in a rotating porous layer during alloy solidification—*Journal of Porous Media*, in press (2002)	Nov. 2001
990	Okhuysen, B. S., and D. N. Riahi	Effect of Coriolis force on instabilities of liquid and mushy regions during alloy solidification—*Physics of Fluids* (submitted)	Dec. 2001
991	Christensen, K. T., and R. J. Adrian	Measurement of instantaneous Eulerian acceleration fields by particle-image accelerometry: Method and accuracy—*Experimental Fluids* (submitted)	Dec. 2001
992	Liu, M., and K. J. Hsia	Interfacial cracks between piezoelectric and elastic materials under in-plane electric loading—*Journal of the Mechanics and Physics of Solids* **51**, 921–944 (2003)	Dec. 2001
993	Panat, R. P., S. Zhang, and K. J. Hsia	Bond coat surface rumpling in thermal barrier coatings—*Acta Materialia* **51**, 239–249 (2003)	Jan. 2002
994	Aref, H.	A transformation of the point vortex equations—*Physics of Fluids* **14**, 2395–2401 (2002)	Jan. 2002
995	Saif, M. T. A, S. Zhang, A. Haque, and K. J. Hsia	Effect of native Al_2O_3 on the elastic response of nanoscale aluminum films—*Acta Materialia* **50**, 2779–2786 (2002)	Jan. 2002
996	Fried, E., and M. E. Gurtin	A nonequilibrium theory of epitaxial growth that accounts for surface stress and surface diffusion—*Journal of the Mechanics and Physics of Solids* **51**, 487–517 (2003)	Jan. 2002
997	Aref, H.	The development of chaotic advection—*Physics of Fluids* **14**, 1315–1325 (2002); see also *Virtual Journal of Nanoscale Science and Technology*, 11 March 2002	Jan. 2002
998	Christensen, K. T., and R. J. Adrian	The velocity and acceleration signatures of small-scale vortices in turbulent channel flow—*Journal of Turbulence*, in press (2002)	Jan. 2002
999	Riahi, D. N.	Flow instabilities in a horizontal dendrite layer rotating about an inclined axis—*Proceedings of the Royal Society of London A*, in press (2003)	Feb. 2002
1000	Kessler, M. R., and S. R. White	Cure kinetics of ring-opening metathesis polymerization of dicyclopentadiene—*Journal of Polymer Science A* **40**, 2373–2383 (2002)	Feb. 2002
1001	Dolbow, J. E., E. Fried, and A. Q. Shen	Point defects in nematic gels: The case for hedgehogs—*Proceedings of the National Academy of Sciences* (submitted)	Feb. 2002
1002	Riahi, D. N.	Nonlinear steady convection in rotating mushy layers—*Journal of Fluid Mechanics* **485**, 279–306 (2003)	Mar. 2002
1003	Carlson, D. E., E. Fried, and S. Sellers	The totality of soft-states in a neo-classical nematic elastomer—*Proceedings of the Royal Society A* (submitted)	Mar. 2002
1004	Fried, E., and R. E. Todres	Normal-stress differences and the detection of disclinations in nematic elastomers—*Journal of Polymer Science B: Polymer Physics* **40**, 2098–2106 (2002)	June 2002
1005	Fried, E., and B. C. Roy	Gravity-induced segregation of cohesionless granular mixtures—*Lecture Notes in Mechanics*, in press (2002)	July 2002
1006	Tomkins, C. D., and R. J. Adrian	Spanwise structure and scale growth in turbulent boundary layers—*Journal of Fluid Mechanics* (submitted)	Aug. 2002
1007	Riahi, D. N.	On nonlinear convection in mushy layers: Part 2. Mixed oscillatory and stationary modes of convection—*Journal of Fluid Mechanics* (submitted)	Sept. 2002
1008	Aref, H., P. K. Newton, M. A. Stremler, T. Tokieda, and D. L. Vainchtein	Vortex crystals—*Advances in Applied Mathematics* **39**, in press (2002)	Oct. 2002

List of Recent TAM Reports (cont'd)

No.	*Authors*	*Title*	*Date*
1009	Bagchi, P., and S. Balachandar	Effect of turbulence on the drag and lift of a particle—*Physics of Fluids* (submitted)	Oct. 2002
1010	Zhang, S., R. Panat, and K. J. Hsia	Influence of surface morphology on the adhesive strength of aluminum/epoxy interfaces—*Journal of Adhesion Science and Technology* (submitted)	Oct. 2002
1011	Carlson, D. E., E. Fried, and D. A. Tortorelli	On internal constraints in continuum mechanics—*Journal of Elasticity*, in press (2003)	Oct. 2002
1012	Boyland, P. L., M. A. Stremler, and H. Aref	Topological fluid mechanics of point vortex motions—*Physica D* **175**, 69–95 (2002)	Oct. 2002
1013	Bhattacharjee, P., and D. N. Riahi	Computational studies of the effect of rotation on convection during protein crystallization—*Journal of Crystal Growth* (submitted)	Feb. 2003
1014	Brown, E. N., M. R. Kessler, N. R. Sottos, and S. R. White	*In situ* poly(urea-formaldehyde) microencapsulation of dicyclopentadiene—*Journal of Microencapsulation* (submitted)	Feb. 2003
1015	Brown, E. N., S. R. White, and N. R. Sottos	Microcapsule induced toughening in a self-healing polymer composite—*Journal of Materials Science* (submitted)	Feb. 2003
1016	Kuznetsov, I. R., and D. S. Stewart	Burning rate of energetic materials with thermal expansion—*Combustion and Flame* (submitted)	Mar. 2003
1017	Dolbow, J., E. Fried, and H. Ji	Chemically induced swelling of hydrogels—*Journal of the Mechanics and Physics of Solids*, in press (2003)	Mar. 2003
1018	Costello, G. A.	Mechanics of wire rope—Mordica Lecture, Interwire 2003, Wire Association International, Atlanta, Georgia, May 12, 2003	Mar. 2003
1019	Wang, J., N. R. Sottos, and R. L. Weaver	Thin film adhesion measurement by laser induced stress waves—*Journal of the Mechanics and Physics of Solids* (submitted)	Apr. 2003
1020	Bhattacharjee, P., and D. N. Riahi	Effect of rotation on surface tension driven flow during protein crystallization—*Microgravity Science and Technology* (submitted)	Apr. 2003
1021	Fried, E.	The configurational and standard force balances are not always statements of a single law—*Proceedings of the Royal Society* (submitted)	Apr. 2003
1022	Panat, R. P., and K. J. Hsia	Experimental investigation of the bond coat rumpling instability under isothermal and cyclic thermal histories in thermal barrier systems—*Proceedings of the Royal Society of London A* (submitted)	May 2003
1023	Fried, E., and M. E. Gurtin	A unified treatment of evolving interfaces accounting for small deformations and atomic transport: grain-boundaries, phase transitions, epitaxy—*Advances in Applied Mechanics*, in press (2003)	May 2003
1024	Dong, F., D. N. Riahi, and A. T. Hsui	On similarity waves in compacting media—*Advances in Mathematics Research* (submitted)	May 2003
1025	Liu, M., and K. J. Hsia	Locking of electric field induced non-180° domain switching and phase transition in ferroelectric materials upon cyclic electric fatigue—*Applied Physics Letters* (submitted)	May 2003
1026	Liu, M., K. J. Hsia, and M. Sardela Jr.	In situ X-ray diffraction study of electric field induced domain switching and phase transition in PZT-5H—*Journal of the American Ceramics Society* (submitted)	May 2003
1027	Riahi, D. N.	On flow of binary alloys during crystal growth—*Recent Research Development in Crystal Growth*, in press (2003)	May 2003
1028	Riahi, D. N.	On fluid dynamics during crystallization—*Recent Research Development in Fluid Dynamics* (submitted)	July 2003
1029	Fried, E., V. Korchagin, and R. E. Todres	Biaxial disclinated states in nematic elastomers—*Journal of Chemical Physics* (submitted)	July 2003